

Relative Permeability Variation Depending on Viscosity Ratio and Capillary Number

Natanael Suwandi^{1,1}, Fei Jiang^{2,2}, and Takeshi Tsuji^{1,1}

¹Kyushu University

²Yamaguchi University

November 30, 2022

Abstract

The relative roles of parameters governing relative permeability, a crucial property for two-phase fluid flows, are incompletely known. To characterize the influence of viscosity ratio (M) and capillary number (Ca), we calculated relative permeabilities of nonwetting fluids (knw) and wetting fluids (kw) in a 3D model of Berea sandstone under steady-state condition using the lattice Boltzmann method. We show that knw increases and kw decreases as M increases due to the lubricating effect, locally occurred pore-filling behavior, and instability at fluid interfaces. We also show that knw decreases markedly at low Ca ($\log Ca < -1.25$), whereas kw undergoes negligible change with changing Ca . An M - Ca - knw correlation diagram, displaying the simultaneous effects of M and Ca , shows that they cause knw to vary by an order of magnitude. The color map produced is useful to provide accurate estimates of knw in reservoir-scale simulations and to help identify the optimum properties of the immiscible fluids to be used in a geologic reservoir.

1 **Relative Permeability Variation Depending on Viscosity Ratio and Capillary Number**

2 **Natanael Suwandi¹, Fei Jiang^{2,3}, Takeshi Tsuji^{1,2,4}**

3 ¹Department of Cooperative Program for Resources Engineering, Graduate School of
4 Engineering, Kyushu University, Fukuoka 819-0395, Japan

5 ²International Institute for Carbon-Neutral Energy Research, Kyushu University, Fukuoka 819-
6 0395, Japan

7 ³Department of Mechanical Engineering, Graduate School of Sciences and Technology for
8 Innovation, Yamaguchi University, Yamaguchi 755-8611, Japan

9 ⁴Department of Earth Resources Engineering, Faculty of Engineering, Kyushu University,
10 Fukuoka 819-0395, Japan

11 Corresponding author: Takeshi Tsuji (tsuji@mine.kyushu-u.ac.jp)

13 **Key Points:**

- 14 • Relative permeability in two-phase flow is calculated in a three-dimensional digital Berea
15 rock using Lattice Boltzmann Method
- 16 • Relative permeability varies due to lubrication effect, shear force and capillary force, and
17 is related to fluid droplet fragmentation
- 18 • Relative permeability on viscosity ratio-capillary number map is created to predict
19 spatiotemporal variation of reservoir permeability

20

21

22

23

24

25

26

27

28

29

30

31 Abstract

32 The relative roles of parameters governing relative permeability, a crucial property for two-phase
33 fluid flows, are incompletely known. To characterize the influence of viscosity ratio (M) and
34 capillary number (Ca), we calculated relative permeabilities of nonwetting fluids (k_{nw}) and
35 wetting fluids (k_w) in a 3D model of Berea sandstone under steady-state condition using the
36 lattice Boltzmann method. We show that k_{nw} increases and k_w decreases as M increases due to the
37 lubricating effect, locally occurred pore-filling behavior, and instability at fluid interfaces. We
38 also show that k_{nw} decreases markedly at low Ca ($\log Ca < -1.25$), whereas k_w undergoes
39 negligible change with changing Ca . An M - Ca - k_{nw} correlation diagram, displaying the
40 simultaneous effects of M and Ca , shows that they cause k_{nw} to vary by an order of magnitude.
41 The color map produced is useful to provide accurate estimates of k_{nw} in reservoir-scale
42 simulations and to help identify the optimum properties of the immiscible fluids to be used in a
43 geologic reservoir.

44 Plain Language Summary

45 The relative permeability is a crucial parameter in a system where two fluid phases exist
46 simultaneously. For example, in carbon capture and storage, relative permeability is important to
47 assess the replacement mechanism of the existing fluid in the reservoir (wetting fluid) by the
48 injected CO₂ (non-wetting fluid). It is also an important parameter in enhanced oil recovery
49 fields, as high relative permeability of oil indicates that the oil in the reservoir can be extracted
50 quickly. The relative permeability is temporally and spatially varied by reservoir conditions (e.g.,
51 temperature). But currently, in reservoir-scale fluid flow simulation, relative permeability is
52 assumed to be constant regardless of the different conditions. In this study, we conducted

53 simulations to calculate relative permeability in various viscosity ratio (M) and capillary number
54 (Ca) conditions. We found that relative permeability changes dramatically in different M and Ca
55 conditions, and we further mapped relative permeability on the diagram between M and Ca to
56 predict relative permeability accurately in various reservoir conditions. Our findings can be
57 useful to determine the suitable fluid properties to be used in reservoir management and to
58 accurately estimate fluid behavior based on reservoir-scale simulation with variant relative
59 permeability.

60 **1 Introduction**

61 The relative permeability of the different fluids in a two-phase flow has been extensively
62 studied in scientific and engineering fields concerned with two-phase flows in geological
63 reservoirs, such as in carbon capture and storage (CCS) fields, enhanced oil recovery (EOR)
64 operations, geothermal power systems, and geological radioactive waste disposal repositories
65 (Benson et al., 2015; C. Chen & Zhang, 2010; Gudjonsdottir et al., 2015; Niibori et al., 2011;
66 Shad et al., 2008; Wu & Wang, 2020). Relative permeability is a crucial hydraulic property for
67 modeling the flow of both fluids and assessing the mechanisms of fluid displacement in the
68 reservoir. For example, when CO₂ is injected into a CCS reservoir, the CO₂ (nonwetting phase)
69 displaces the existing fluid in the reservoir, such as oil or brine (wetting phase). Relative
70 permeability values can be used to estimate the reduction in CO₂ fluid flow due to surface-
71 tension effects between CO₂ and the brine, thus the parameter is useful to assess the injectivity of
72 the CO₂ (Benson et al., 2015; Burnside & Naylor, 2014). The relative permeability can also aid
73 estimation of how much fluid can be displaced by CO₂ before the system reaches the wetting
74 fluid irreducible saturation condition, limiting the CO₂ volume that can be stored in the reservoir

75 (Burnside & Naylor, 2014). Conversely, in EOR systems, the best results are obtained when the
76 relative permeability is high for oil and low for the injected fluid (Heins et al., 2014).

77 Several factors influence relative permeability in a two-phase flow system. For example,
78 in a CCS project, the fluid relative permeability is affected by the heterogeneity of the rock, such
79 as pore size and pore connectivity (Benson et al., 2015; Fei Jiang & Tsuji, 2014; Zhang et al.,
80 2022). In addition, relative permeability is affected by the interactions between the two fluids,
81 such as interfacial tension, the viscosity and velocity of the fluids, and their wettability (Lefebvre
82 du Prey, 1973). Because fluid viscosity varies dramatically with pressure and temperature, such
83 reservoir environments can further affect relative permeability. Therefore, in a two-phase flow
84 system, the relative permeability value of each fluid is not only a function of saturation; it is also
85 affected by other parameters related to environmental and by the interaction between the two
86 component fluids.

87 Lenormand et al. (1988) reported that two parameters, viscosity ratio and capillary
88 number, can explain the interaction between two immiscible fluids. The viscosity ratio (M) is a
89 dimensionless parameter describing the ratio between the viscosity of the injected nonwetting
90 fluid and the viscosity of the ambient wetting fluid:

$$91 \quad M = \frac{\mu_{nw}}{\mu_w} \quad (1)$$

92 where μ_{nw} is the dynamic viscosity of the nonwetting fluid and μ_w is the dynamic viscosity of the
93 wetting fluid.

94 The capillary number (Ca) is a dimensionless parameter describing the ratio between the
95 viscous drag forces and the interfacial tension forces between two immiscible fluids:

96
$$Ca = \frac{\mu_{nw} V_{nw}}{\sigma} \quad (2)$$

97 where V_{nw} is the average fluid velocity of the nonwetting fluid and σ is the interfacial tension
98 (IFT) between the two fluids.

99 Despite the recognition that the relative permeability k is a function of M , several studies
100 of this relationship have reported divergent results. An experimental study (Odeh, 1959) found
101 that the relative permeability of the nonwetting fluid (k_{nw}) increases and the relative permeability
102 of the wetting fluid (k_w) stays relatively constant as M increases, as have several other
103 experimental and numerical studies (Dou & Zhou, 2013; Goldsmith & Mason, 1963; Huang &
104 Lu, 2009; Jeong et al., 2017; Mahmoudi et al., 2017; Yiotis et al., 2007; Zhao et al., 2017). An
105 analytical study of co-current annular flow in which the wetting fluid is distributed on the pore
106 surface and the nonwetting fluid is in the middle of the pore produced empirical equations for the
107 nonwetting and wetting fluids as a function of M and saturation:

108
$$k_{nw} = S_{nw} \left[\frac{3}{2} M + S_{nw}^2 \left(1 - \frac{3}{2} M \right) \right] \quad (3)$$

109
$$k_w = \frac{1}{2} (1 - S_w)^2 (3 - S_w) \quad (4)$$

110 where S_{nw} is the saturation of the nonwetting fluid, and $S_w = 1 - S_{nw}$ is the saturation of the
111 wetting fluid. These equations suggest that k_w is not affected by increasing M and is a function of
112 saturation alone. However, other studies have reported that k_{nw} increases and k_w decreases as M
113 increases (Ahmadlouydarab et al., 2012; Fan et al., 2019; Goel et al., 2016; Ramstad et al.,
114 2010); thus, there is as yet no general agreement on the variation of k_w with increasing M . One of
115 the challenges of previous studies was the difficulty of removing the effects of capillary forces
116 and wettability factors when evaluating this relationship.

117 Similarly, studies of the influence of Ca on relative permeability is still incompletely
118 known. In an experimental study, Fulcher et al. (1985) concluded that k_{nw} is a function of IFT
119 and viscosity variables individually rather than a function of the Ca , whereas k_w can be modeled
120 directly as a function of Ca . Several studies (Asar & Handy, 1989; Fan et al., 2019; Harbert,
121 1983) also found that both k_{nw} and k_w increase as IFT decreases because the two fluids interfere
122 less with each other and thus tend to form more well-connected flow pathways. One of the
123 studies (Asar & Handy, 1989) showed that both fluids relative permeability curves tend to
124 straighten and approach the 45° tangent line as IFT approaches zero. Other studies (Amaefule &
125 Handy, 1982; Fei Jiang et al., 2014; Shen et al., 2010) also concluded that both k_{nw} and k_w
126 decrease as Ca decreases. On the other hand, a numerical study (Zhao et al., 2017) concluded
127 that k_w increases with increasing Ca under neutral wetting conditions ($\theta = 90^\circ$) but stays
128 relatively constant with increasing Ca under strong wetting conditions ($\theta = 135^\circ$). These
129 divergent results warrant further investigations of how relative permeability changes with
130 changing IFT and Ca . One of the challenges in this evaluation is the difficulty of isolating the
131 effect of IFT while keeping other parameters, such as viscosity, constant. In addition, Ca is a
132 function of fluid velocity, which is a direct of from the simulation. Thus, it is difficult to hold Ca
133 constant in all simulation conditions.

134 Previous studies have also demonstrated how the viscosity ratio can affect the breakup of
135 fluid droplets. Instabilities due to the viscosity gradient at the interface of the two fluids cause
136 fluid droplet deformation and breakup under viscous flow conditions when the Reynolds number
137 is low (Bischofberger et al., 2015; Mu'min et al., 2021; Nekouei & Vanapalli, 2017; Stone,
138 1994). We suspect that the fluid droplet fragmentation mechanism is also one of the driving
139 factors of the relative permeability change caused by the viscosity ratio. However, to the best of

140 our knowledge, no research linking relative permeability variation to fluid droplet breakup
141 caused by viscosity ratio variation has ever been done.

142 Previous studies have usually evaluated the separate effects of M and Ca on relative
143 permeability. However, in two-phase flows, the effects of viscosity gradient and interfacial
144 tension must be evaluated simultaneously to accurately predict the hydraulic properties in the
145 system (Tsuji et al., 2016), including relative permeability. Because few studies have evaluated
146 the condition when both parameters influence relative permeability using a steady-state
147 simulation, our aim in this work was to fill that knowledge gap.

148 In this paper, we propose a method to simultaneously evaluate the effects of viscosity
149 ratio M and capillary number Ca on relative permeability by creating a $M-Ca-k_{nw}$ relationship
150 map (i.e., showing relative permeability on a diagram relating M and Ca) by applying a color
151 gradient Lattice Boltzmann method (LBM) simulation to a three-dimensional (3D) digital rock
152 model. We begin by evaluating the effects of M and Ca individually on the relative
153 permeabilities of the nonwetting and wetting fluids by holding other parameters constant. We
154 also calculate the number of fluid clusters to describe the fluid connectedness, a factor that is
155 directly related to relative permeability, and link the fluid connectedness to fluid droplet breakup.
156 We then map k_{nw} for various $M-Ca$ conditions in search of general trends. We believe that such a
157 map has never before been created, and that it will be useful for quickly estimating relative
158 permeability if M and Ca are known. By understanding the variations of relative permeability in
159 the $M-Ca$ parameter space, we can conduct accurate large-scale reservoir simulations by
160 considering the reservoir conditions M and Ca and thereby contribute to the wide range of
161 research regarding applications that employ two-phase fluid mixtures.

162 **2 Methods**

163 2.1 Lattice Boltzmann Method

164 The LBM is a branch of computational fluid dynamics that has emerged as a popular
165 technique to solve multiphase fluid flow systems in complex geometries because of its
166 algorithmic simplicity (S. Chen & Doolen, 1998; Dou & Zhou, 2013; Fei Jiang et al., 2014;
167 Ramstad et al., 2010; Succi et al., 2010). LBM simulations treat fluids as a group consisting of
168 fictive particles; the movement of these particles is simulated with a statistical approach. The
169 movement of the bulk fluid is simulated from the propagation and collision processes of the
170 fictive particles (Huang et al., 2011). We chose the Rothman–Keller color gradient model (Tölke
171 et al., 2006) to conduct the simulations because it can simulate a high fluid viscosity ratio with
172 better accuracy than other LBM models (Ahrenholz et al., 2008; Yang & Boek, 2013). The color
173 gradient model is so named because it graphically represents two-phase fluids as a mixture of a
174 wetting and nonwetting fluid, assigned the colors blue and red, respectively (Huang et al., 2015;
175 Fei Jiang et al., 2022). Our 3D simulations used the D3Q19 (3 dimensions, 19 velocity lattice)
176 velocity model.

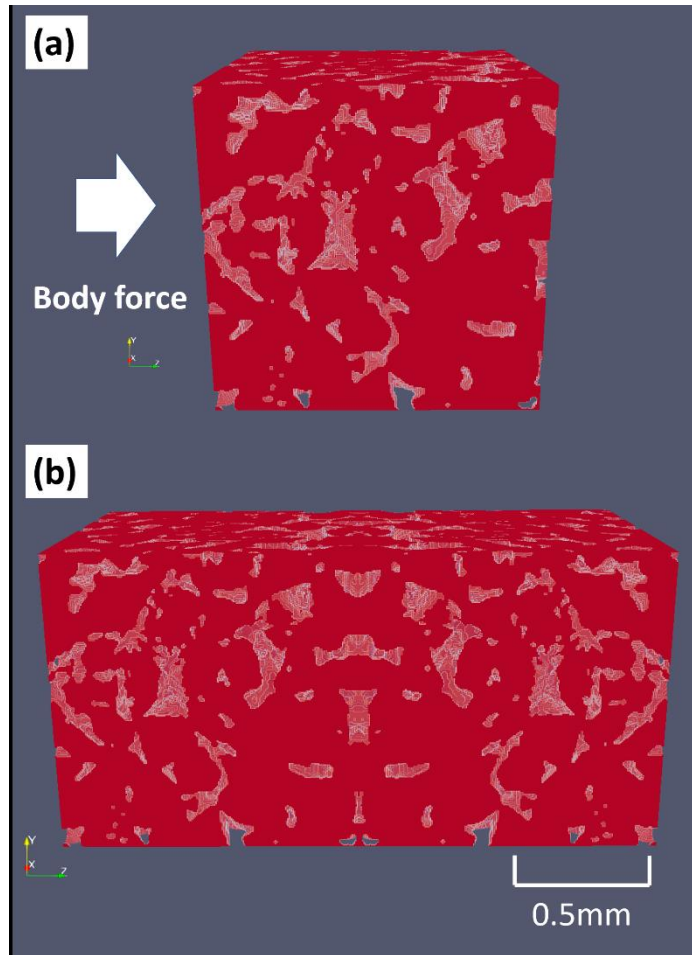


Fig. 1. Berea sandstone digital rock model: (a) core form and (b) mirrored form.

177

178 2.2 Digital rock model

179 We used a 3D digital rock model obtained from microtomographic images of Berea
180 sandstone (Fig. 1a). Berea sandstone is chosen due to its relatively well-known properties (Øren
181 & Bakke, 2003). The rock has a relatively large mean grain size of $\sim 250 \mu\text{m}$ and consists of
182 quartz, feldspar, carbonates, and clay minerals. Its average pore size is $\sim 20 \mu\text{m}$ with an average
183 throat size of $\sim 10 \mu\text{m}$. Our rock model, obtained from the database of Dong and Blunt (2009),
184 had an original resolution of $5.345 \mu\text{m}$ per pixel. To ensure that the digital rock resolution would
185 be fine enough for the two-phase flow simulation conditions, each pixel was split into 2; hence,

186 each pixel in our model represents 2.673 μm . The 3D digital rock is a stack of 400 tomographic
 187 images, and each image includes 400×400 pixels. Thus, the digital rock represents an actual
 188 size of 1.069 mm \times 1.069 mm \times 1.069 mm. The simulation requires a rock model that is larger
 189 than its representative elementary volume (~ 1 mm for Berea sandstone), and the multi-pore
 190 nature of the rock must be considered.

191 2.3 Relative permeability calculation

192 The viscosity ratio M is defined by dividing the nonwetting fluid's viscosity (μ_{nw}) by the
 193 wetting fluid's viscosity (μ_{w}) (equation 1). In the LBM, μ can be calculated as follows:

$$194 \quad \mu = \frac{1}{3} \left(\tau - \frac{1}{2} \right) \quad (5)$$

195 where τ represents the relaxation parameter. Thus, the viscosities of both fluids can be modified
 196 by changing the τ value. Because τ must be larger than 0.5 for a positive viscosity and the
 197 simulation becomes unstable as τ approaches 0.5, it is important that the simulation uses a τ
 198 value that ensures its stability and accuracy. In this study, we altered M only by changing the τ
 199 value of the nonwetting fluid to manipulate μ_{nw} . The wetting fluid viscosity was kept constant at
 200 0.1555 lu^2/ts (length²/time in lattice units) in all simulations to preserve its stability. Changes in
 201 M can be interpreted as a change in either μ_{w} or μ_{nw} ; thus, modifying either viscosity value will
 202 produce the same results if their ratio is maintained.

203 The capillary number Ca can be modified based on equation (2) by changing the σ and
 204 μ_{nw} parameters. Because μ_{nw} is also used to determine M , we achieved the desired Ca by
 205 adjusting σ alone. In the color gradient LBM model, σ can be modeled by introducing a
 206 perturbation term into equilibrium equations based on the gradient of the phase field of the two

207 fluids. Tölke et al. (2006) provides a detailed description of the model. The average velocity of
208 the nonwetting fluid after the simulation had converged to equilibrium was used to calculate the
209 Ca number. We adjusted σ at every simulation point (every M and in every saturation condition)
210 to ensure that Ca had a similar value and fell within the permitted error range of $\log Ca \pm 0.10$.
211 When the fluid velocity change in the last 1,000 simulation steps was less than 2% for all cases,
212 the simulations were assumed to have converged at that time. The time-averaged velocity value
213 in the last 3,000 steps was calculated for further investigation.

214 To remove the complications arising from wettability effects, we assumed that the solid
215 was completely nonwetting ($\theta = 180^\circ$) to the nonwetting fluid in all conditions. Given that
216 condition, the wetting fluid coats the surface of the rock, whereas the nonwetting fluid is not in
217 contact with the pore wall and can only occupy the central parts of the pores.

218 We applied a steady-state simulation condition, which assumes that the wetting fluid
219 saturation (S_w) and nonwetting fluid saturation (S_{nw}) are kept constant. In the initial state, both
220 fluids were specified as being randomly distributed in the pore spaces. The initial condition was
221 chosen because it allows each pore body to have roughly the same proportions of nonwetting and
222 wetting fluid according to the prescribed saturation; thus, this condition produces an extremely
223 uniform distribution of nonwetting and wetting fluid throughout the rock. In addition, because
224 the initial fluid connectivity is reduced under this initial condition and increases capillary
225 trapping, this initial distribution might be desirable in a CCS site (Fei Jiang & Tsuji, 2016).
226 Under this initial condition, fluids are generated randomly in pore space; therefore, some
227 nonwetting fluids touch the grain surface at the initial stage. As the simulation progresses, the
228 wetting fluid coats the surface of the rock, and the nonwetting fluid moves to occupy only the
229 central parts of pores because of the perfect wettability condition of the solid. A constant body

230 force was applied in the z direction to both fluids to mimic the pressure gradient: $g = dP/dz$ (Fig.
231 1a). For the interaction between rock solid nodes and fluid voxels, no-slip boundary conditions
232 were applied by using the halfway bounce-back scheme (X. Li et al., 2016; Singh et al., 2017).
233 The density of both fluids was set at 1.0 in lattice units, which corresponds to $1,000 \text{ kg/m}^3$ in the
234 physical unit. We did this because our study was focused on viscosity differences, and the effect
235 of density contrast is minor if inertial force can be neglected.

236 We applied a periodic boundary condition in the x , y , and z directions of our 3D model.
237 Specifically, in the flow direction (z direction), the rock was mirrored to ensure that the pore
238 spaces on the right side were connected to the left side of the digital rock (Fig. 1b) (F Jiang &
239 Tsuji, 2017).

240 2.3.1 Relative permeability curve

241 The relative permeability curve is a plot of k versus saturation S_{nw} . As S_{nw} increases, k_{nw}
242 increases and k_w decreases. The shape of this curve can change as a result of viscous drag force
243 and capillary force; thus, an investigation of its variation with changes in M and Ca is important
244 to determine the optimum conditions to achieve the desired value of k . We plotted k_{nw} and k_w as a
245 function of S_{nw} to create relative permeability curves for various conditions.

246 In this study, we plotted all permeability curves for S_{nw} values within a wide range from
247 10% to 90%. Although some of these S_{nw} values might be unrealistic in actual injection settings
248 because of irreducible wetting phase saturation (Tsuji et al., 2016), we still considered those
249 hypothetical S_{nw} conditions for the ideal situation of a steady-state laboratory experiment.

250 2.3.2 M - Ca - k_{nw} permeability color map

251 After confirming the influence of M and Ca on k_{nw} and k_w in a two-phase flow system,
252 we conducted simulations at various M and Ca conditions with S_{nw} held at a constant value of
253 20% to create a plot of M – Ca – k_{nw} correlation or color diagram. The 20% S_{nw} condition was
254 chosen because it can realistically be achieved under all M – Ca conditions (Tsuji et al., 2016).
255 The color diagram is useful to evaluate the degree of influence of M and Ca on changes of
256 relative permeability when both parameters influence a system, and can also provide estimates of
257 relative permeability in a reservoir under a wide range of M and Ca .

258 **3 Results and interpretation**

259 Before conducting simulations in various M and Ca conditions, we first ran single-phase
260 simulations to determine the absolute permeability value of the porous media and to verify the
261 stability of the simulation. The results are presented in Appendix A. Afterwards, the effects of M
262 and Ca were then evaluated individually to see how they influence nonwetting and wetting
263 relative permeability curves in a two-phase flow system. Next, we conducted simulations over a
264 wide range of M and Ca values at a S_{nw} value of 20% to create a relative permeability color
265 diagram.

266 **3.1 Relative permeability curve from a two-phase simulation**

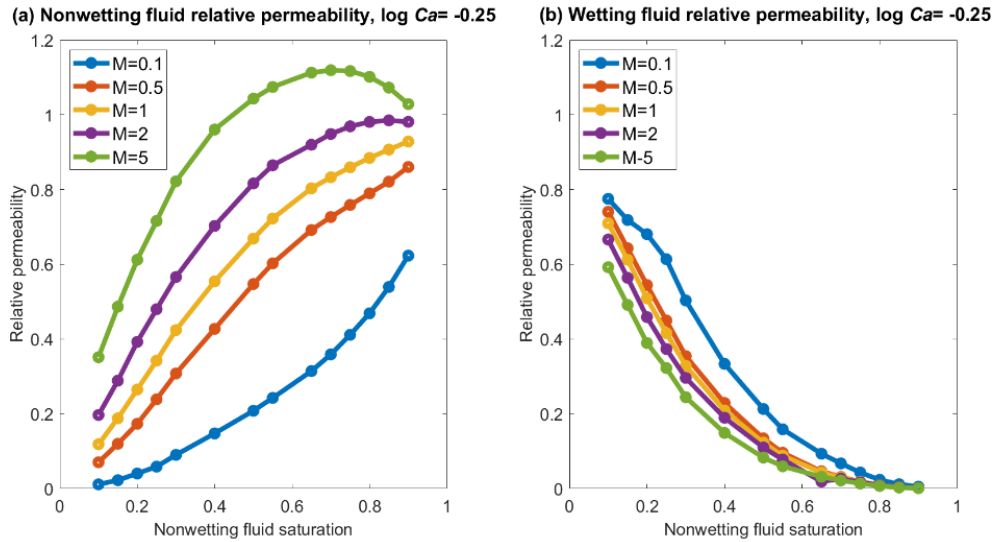


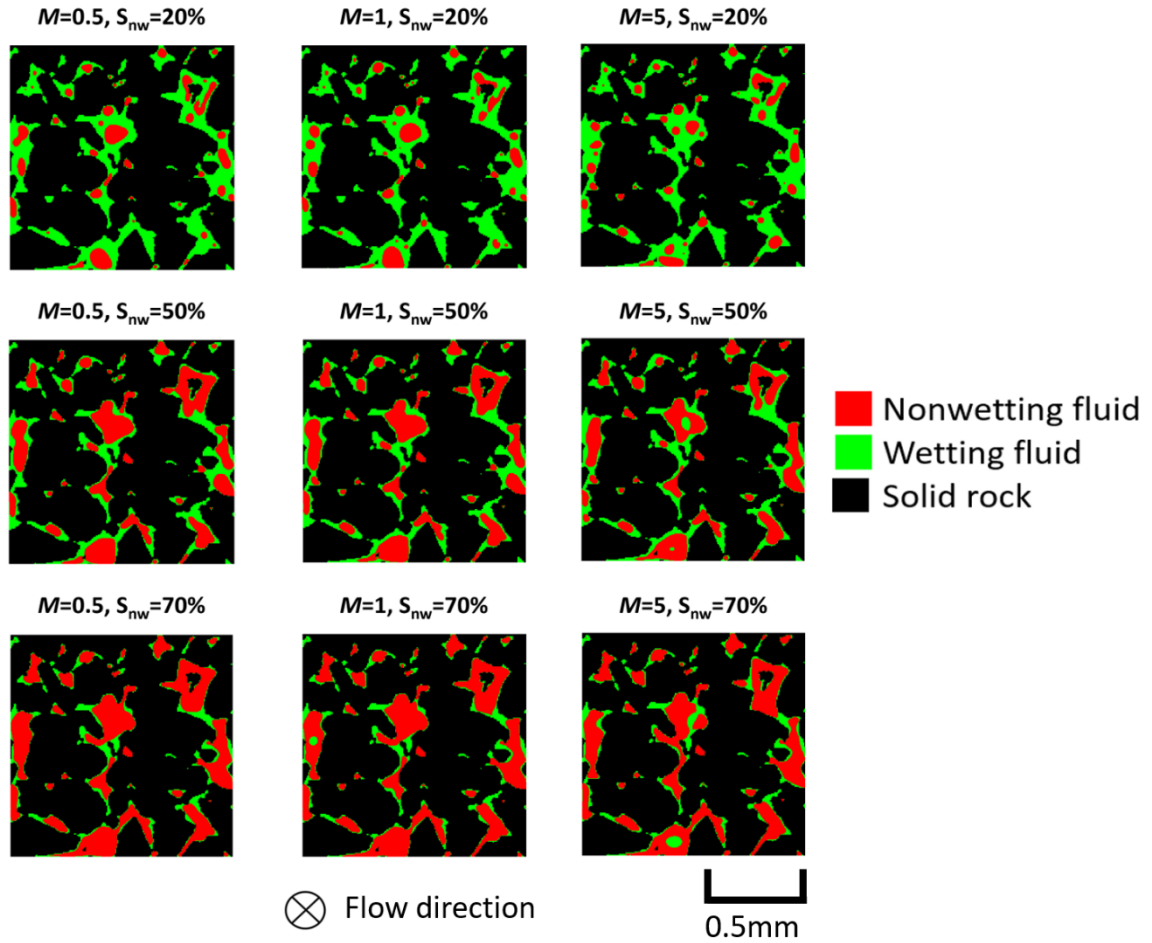
Fig. 2. Relative permeability curves as a function of M at constant $\log Ca = -0.25 \pm 0.1$ for $M = 0.1$ –5: (a) nonwetting fluid relative permeability (k_{nw}) curve and (b) wetting fluid relative permeability (k_w) curve.

267

268 3.1.1 Effect of changes in M on k_{nw} and k_w

269 We plotted values of k_{nw} for five values of M (0.1, 0.5, 1, 2, and 5) over the range of S_{nw}
 270 (10% to 90%) while holding $\log Ca$ nearly constant at -0.25 ± 0.10 (Fig. 2a). We evaluated the
 271 two-phase flow at high Ca to completely remove the capillary force effect. In all simulation
 272 conditions, the Reynolds number must not exceed 10 (Bear, 1975). The maximum Reynolds
 273 number reached in this set of simulations was 5.27 and 9.50 for nonwetting and wetting fluid,
 274 respectively. The M values (0.1, 0.5, 1, 2, and 5) were chosen to represent a wide range of
 275 mobility conditions, from an extremely unfavorable to an extremely favorable mobility
 276 condition. The k_{nw} value increased as M increased, especially for intermediate S_{nw} values (30% to
 277 70%). For $M = 5$, k_{nw} exceeded 1 under some S_{nw} conditions; that is, it exceeded the intrinsic
 278 permeability of the rock. This result agrees with previous studies and can be explained by the

279 lubrication effect, also known as the viscous coupling effect (Goel et al., 2016; Fei Jiang et al.,
 280 2021; H. Li et al., 2005; Ramstad et al., 2010; Yiotis et al., 2007; Zhao et al., 2017).



281 Fig. 3. Two-dimensional slice showing the distributions of nonwetting fluid (red), wetting fluid (green),
 282 and solid rock (black) at various values of M and S_{nw} .

282 To illustrate the lubrication effect, we provide a 2D image showing the distribution of
 283 nonwetting fluid, wetting fluid, and solid rock at the final state of the simulation under various M
 284 and S_{nw} conditions (Fig. 3). Because the wetting fluid (green) layer is generally present between
 285 the nonwetting fluid and the rock, the wetting fluid moves along the rock surface and the
 286 nonwetting phase is confined to the central part of the pore. Thus, the velocity of the nonwetting

287 fluid is affected only by the momentum transfer across fluid–fluid interfaces and not by contact
288 with the grain surface.

289 At sufficiently high values of M , the wetting fluid acts as a lubricant that enhances the
290 movement of the nonwetting fluid, making its permeability higher than in the single-phase
291 condition such that k_{nw} is greater than 1 (Fig. 2a). This lubrication effect most strongly affects
292 k_{nw} in the intermediate S_{nw} range, when the wetting fluid forms thick films that provide the
293 nonwetting fluid with a moving boundary (Vafai, 2000). At low S_{nw} , the nonwetting phase tends
294 to form droplets with low connectivity; thus, the lubrication effect is less pronounced. At high
295 S_{nw} , k_{nw} also decreases toward unity because less wetting fluid is present in the rock and the
296 nonwetting phase comes into contact with the rock, degrading the lubrication effect and reducing
297 k_{nw} near to the single-phase condition. Because the lubrication effect occurs at high M values, it
298 is commonly observed in mixtures of heavy oil and water in EOR systems and has been
299 confirmed by experimental results (Goel et al., 2016; Shad et al., 2008).

300 In addition to the lubrication effect, the relative permeability change due to the viscosity
301 ratio can be linked to local pore-filling behavior. Because of the body force, a nonwetting fluid
302 droplet can move from one pore body to neighboring pore bodies. As M increases, as a result of
303 favorable mobility conditions, there is more chance for nonwetting fluid droplets to move to
304 several neighboring pore bodies through the narrow pore throats (Bakhshian et al., 2021),
305 causing fluid droplet fragmentation and thereby enabling the fluid to occupy smaller pore spaces.
306 This might be one of the contributing factors causing k_{nw} to exceed 1 when $M = 5$ at intermediate
307 saturation. Furthermore, under high S_{nw} , nonwetting fluid already exists in most of the pore
308 bodies throughout the simulation time; thus, locally occurring pore-filling behavior effects
309 decrease, causing k_{nw} to decrease towards unity under high S_{nw} conditions.

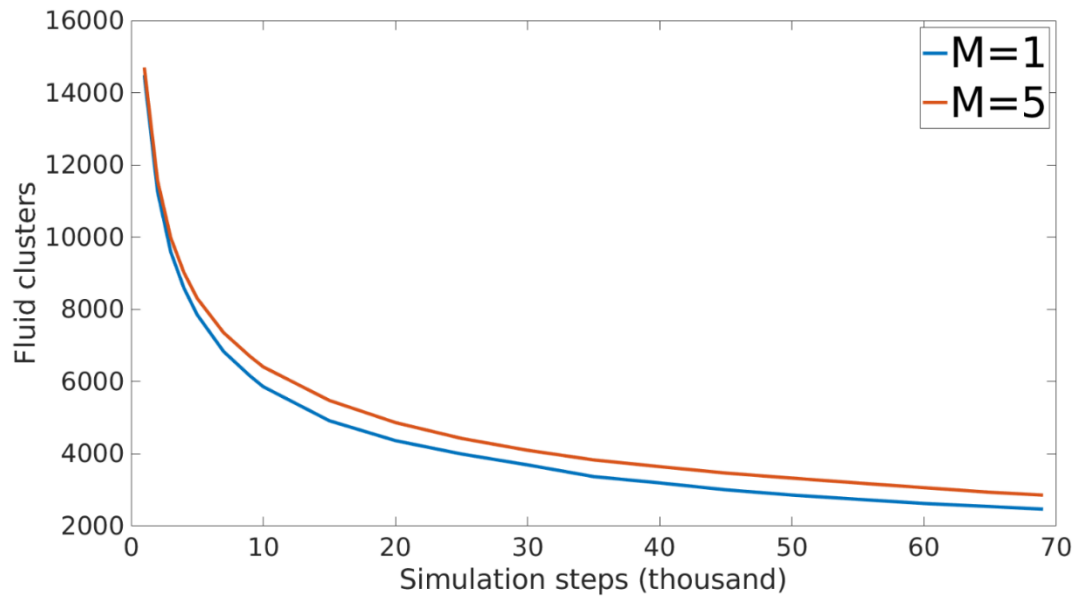


Fig. 4. Evolution of the number of clusters of nonwetting fluid at $M = 1$ and $M = 5$, with $S_{nw} = 20\%$ and $\log Ca = -0.25 \pm 0.1$.

310

311

312

313

314

315

316

317

318

319

320

321

322

323

To investigate nonwetting fluid droplet fragmentation throughout the simulation, we considered the evolution of the number of nonwetting fluid clusters during simulations with $M = 1$ and $M = 5$, $\log Ca = -0.25 \pm 0.10$, and $S_{nw} = 20\%$ (Fig. 4). Throughout the simulations, the number of nonwetting clusters for both simulation conditions decreases, suggesting that some of the nonwetting fluid clusters become more connected and form larger clusters as the simulation proceeds. In the final converged condition, the number of nonwetting fluid clusters is higher for $M = 5$ than for $M = 1$. This result indicates that the nonwetting fluid at $M = 5$ forms more individual clusters and has less fluid connectivity than at $M = 1$. This difference is the result of the instability of the interface of the fluids due to the viscosity stratification (Yiantsios & Higgins, 1988; Yih, 1967). When two immiscible fluids have different viscosities, their velocities will also be different at their interface, causing instability. The instability causes the nonwetting fluid to create more clusters. This result agrees with past research and our hypothesis that instability at the fluid interface can cause fluid droplet fragmentation (Bischofberger et al.,

324 2015; Mu'min et al., 2021; Nekouei & Vanapalli, 2017; Stone, 1994). As more fluid clusters are
 325 formed, the size of the nonwetting fluid clusters is smaller, and it is easier for them to pass
 326 through the pore space. At $M = 1$, the nonwetting fluid is more connected and its fluid clusters
 327 are larger. The larger clusters cannot pass through the small pore throats, leading to lower k_{nw} .

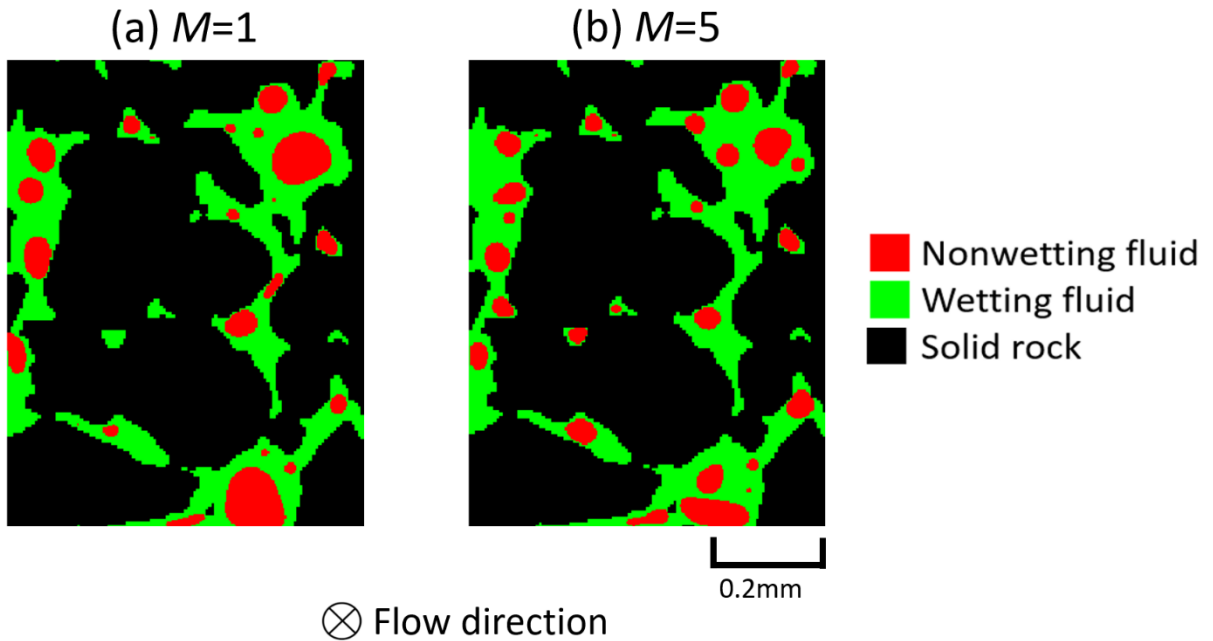


Fig. 5. Two-dimensional slice showing the distributions of nonwetting (red), wetting fluid (green), and solid rock (black) at (a) $M = 1$ and (b) $M = 5$ at 20% S_{nw} . These images show a portion of the slice illustrated in Fig. 3.

328

329 To obtain further insights into fluid cluster size, we provide an illustration showing
 330 nonwetting and wetting fluid distributions in an enlarged section of a 2D slice of the simulated
 331 specimen for $M = 1$ and $M = 5$ at $\log Ca = -0.25 \pm 0.10$ and 20% saturation after the simulation
 332 had converged (Fig. 5). The nonwetting fluid (red) at $M = 1$ forms larger clusters in the pore
 333 throat, whereas at $M = 5$, the nonwetting fluid forms a larger number of clusters but the size of
 334 each cluster is smaller. This result is comparable to our findings (shown in Fig. 4) that
 335 nonwetting fluid droplet fragmentation occurs as a result of instability at the fluid interface as M
 336 increases. Because the nonwetting fluid clusters are smaller, it is easier for them to pass through

337 the pore space, leading to higher k_{nw} . Furthermore, the wetting fluid (green) coats the grain
338 surface under both conditions and produces a lubrication effect (Fig. 5).

339 Our results also demonstrate that k_w decreases as M increases (Fig. 2b), mainly when
340 nonwetting fluid saturation is low. This phenomenon can be attributed to an increase of shear
341 force from the nonwetting phase. As M increases and nonwetting fluid droplet fragmentation
342 occurs, the wetting fluid has a larger contact area with the nonwetting fluid (Fig. 5). As a result,
343 the wetting fluid receives a higher shear force from the nonwetting fluid, which inhibits the flow
344 of the wetting fluid so that it has a lower velocity. In addition, as wetting fluid saturation
345 decreases, the k_w gaps under all M conditions become smaller.

346 To confirm our interpretation, we calculated the degree of contact between nonwetting
347 and wetting fluid by calculating the number of wetting fluid voxels that were adjacent to a
348 nonwetting fluid voxel, for conditions of $M = 1$ and $M = 5$ at $\log Ca = -0.25 \pm 0.10$ and $S_{nw} =$
349 20%. When the simulations converged, 13.77679% and 13.88825% of wetting fluid voxels were
350 adjacent to nonwetting fluid voxels at $M = 1$ and $M = 5$, respectively. This result shows that, at M
351 = 5, the wetting phase fluid has a higher degree of contact with the nonwetting fluid and receives
352 more drag force from the nonwetting fluid; thus, k_w is lower at $M = 5$ than at $M = 1$, as shown in
353 Fig. 2b.

354 In addition, Zhao et al. (2017) suggested that the k_w decrease in response to an M increase
355 occurs because the wetting fluid is more attached to the grain surface when the viscosity ratio is
356 large. When the viscosity ratio is high, fragmentation of the nonwetting phase tends to occur
357 easily and the fragments move towards the centers of pore bodies, so that wetting fluid can easily
358 move to coat the grain surface. Consequently, because the wetting fluid has a larger contact area
359 with the grain surface, it receives more shear drag force, which causes a decrease in velocity. To

360 confirm our interpretation, we calculated the degree of contact between the wetting fluid and the
 361 grain surface, as indicated by the number of wetting fluid voxels having a solid surface as a
 362 neighbor, for $M = 1$ and $M = 5$ at $\log Ca = -0.25 \pm 0.10$ and $S_{nw} = 20\% - 70\%$ after the simulation
 363 had converged (Table 1).

| | $M=1$ | $M=5$ |
|---------------|-----------|-----------|
| $S_{nw}=20\%$ | 36.79546% | 36.74534% |
| $S_{nw}=50\%$ | 50.94340% | 51.18913% |
| $S_{nw}=70\%$ | 67.81628% | 68.25865% |

Table 1. Percentage of wetting fluid that has a grain surface as a neighbor voxel fluid at $M = 1$ and $M = 5$, with S_{nw} of 20%–70% and $\log Ca = -0.25 \pm 0.1$, after the simulation has converged.

364

365 At $S_{nw} = 20\%$, the percentage of wetting fluid voxels adjacent to a solid surface is low,
 366 because the wetting fluid film between the nonwetting fluid and grain surface is thick (Fig. 3)
 367 and only a small portion of the wetting fluid is in direct contact with the grain surface. The
 368 values for $M = 1$ and $M = 5$ are also similar, suggesting that the nonwetting fluid at low S_{nw} has
 369 less chance to approach the rock surface because of the thick wetting fluid film even as M
 370 increases. Thus, at low S_{nw} , the dominant cause of the k_w decrease is the shear force at the fluid
 371 interface and not the shear drag force at the wall. When $S_{nw} = 50\%$ and 70% and $M = 5$, the
 372 proportion of the wetting phase fluid attached to the grain surface increases compared to when M
 373 $= 1$, indicating that the wetting fluid has a higher degree of contact and receives more drag force
 374 from the solid wall. Thus, k_w at $M = 5$ is lower than that at $M = 1$ (Fig. 2b).

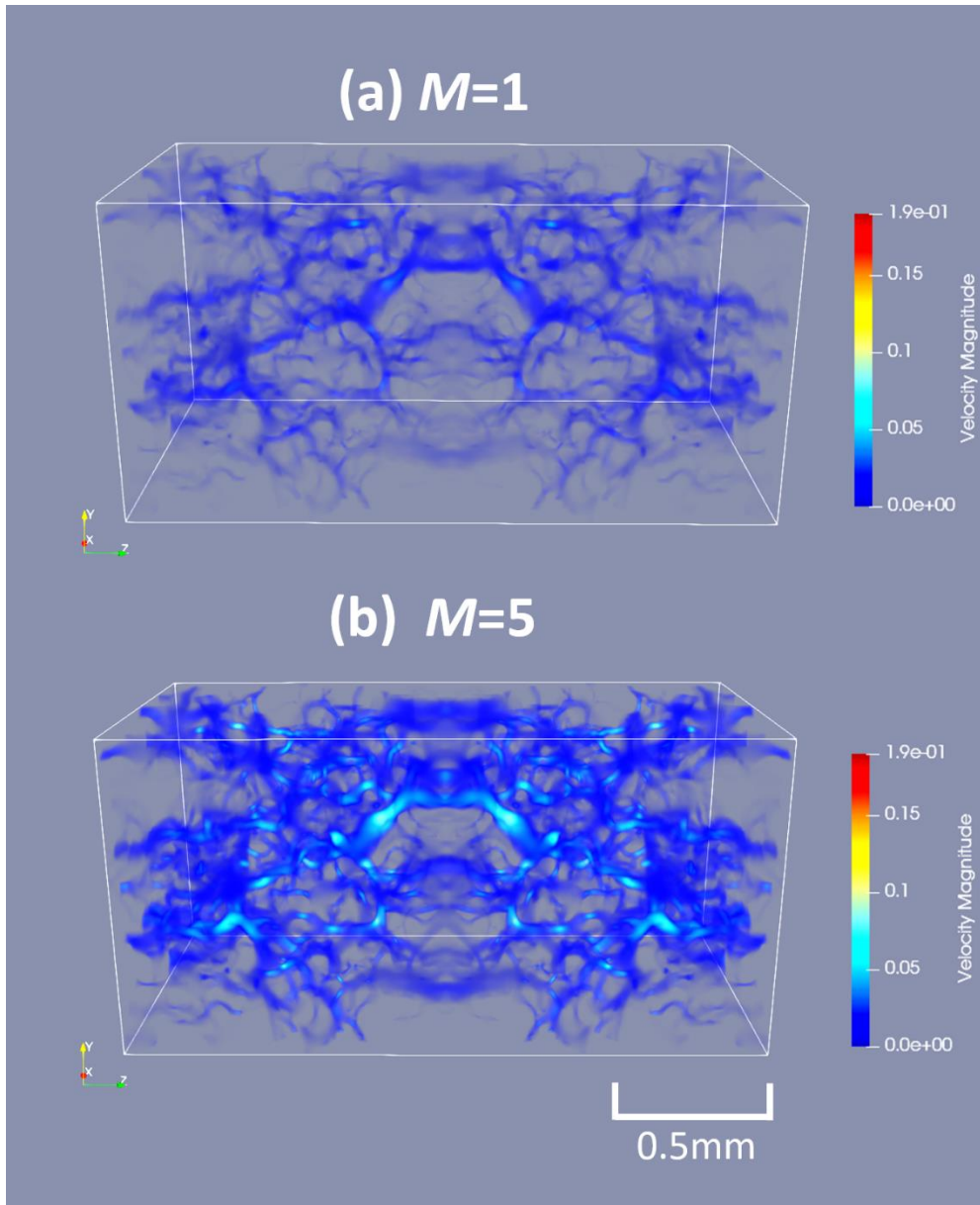


Fig. 6. Normalized velocity fields for the nonwetting fluid in a two-phase simulation with (a) $M = 1$ and (b) $M = 5$, at $\log Ca = -0.25 \pm 0.1$ and $S_{nw} = 20\%$.

375

376 The results of fluid velocity for $M=1$ and $M=5$ in the pore spaces at 20% saturation after
 377 the simulation converges are plotted in Figs. 6a and 6b, respectively. The fluid velocity field in

378 Fig. 6 is normalized to consider the effect of viscosity change using the equation $U^* = \frac{U}{\Delta PL/\mu}$. It

379 can be seen that the normalized fluid velocity is higher at $M = 5$ than at $M = 1$, indicating that k_{nw}
 380 is higher at $M = 5$ than at $M = 1$, in agreement with our relative permeability curve.

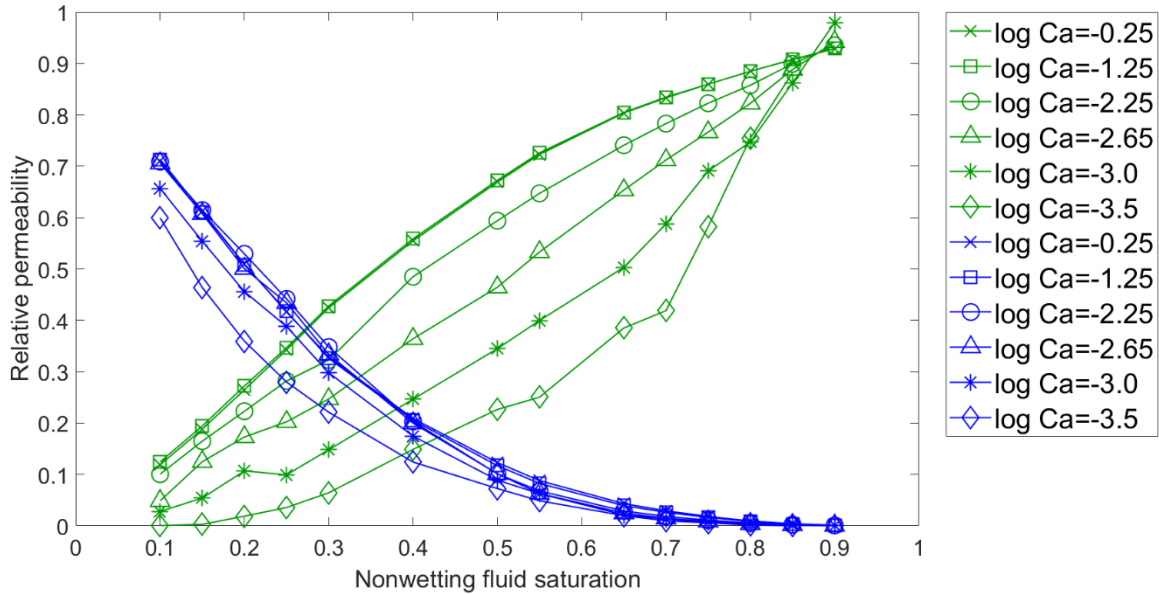


Fig. 7. Relative permeability curves for the nonwetting (k_{nw} , green) and wetting fluids (k_w , blue) for $Ca = -0.25$ to -3.5 with $M = 1$.

381

382 3.1.2 Effect of Ca change on k_{nw} and k_w

383 The k_{nw} and k_w curves for six different values of $\log Ca$ ($-0.25, -1.25, -2.25, -2.65, -$
 384 $3.00, \text{ and } -3.50 \pm 0.10$) at $M = 1$ are plotted (Fig. 7). The Ca value is altered by changing the IFT
 385 value. It was difficult to keep Ca constant because Ca is also a function of fluid velocity, which
 386 is a direct result of the simulation. Thus, we allowed a small error of ± 0.10 for Ca under all
 387 conditions.

388 The k_{nw} values remain relatively constant between $\log Ca = -0.25$ and -1.25 , i.e., for
 389 high Ca /low IFT values, and the relative permeability curve for the nonwetting fluid is an
 390 approximately straight line, in agreement with previous studies (Asar & Handy, 1989; Shen et

391 al., 2010). However, as $\log Ca$ becomes lower than -1.25 , k_{nw} notably decreases as Ca decreases.
392 This decrease occurs because the flow of the nonwetting fluid is more strongly inhibited by
393 capillary force when Ca is low. Capillary force is controlled by IFT, the surface tension forces
394 between the nonwetting and wetting fluids. As IFT increases, the nonwetting fluid becomes
395 trapped by the larger capillary force in the small pore spaces, thus causing k_{nw} to decrease. This
396 result also suggests that k_{nw} does not decrease linearly with changes in IFT/Ca , because the k_{nw}
397 decrease gap gradually becomes larger as Ca decreases. This phenomenon occurs because as Ca
398 becomes lower, the influence of capillary force becomes more dominant.

399 For the wetting fluid, k_w also decreases as Ca decreases (Fig. 7), but at a much smaller
400 rate compared to k_{nw} , consistent with previous research (Harbert, 1983; Fei Jiang et al., 2014;
401 McDougall et al., 2007; Ramstad et al., 2010; Zhao et al., 2017). The reason for this result is that
402 the wetting fluid flows only along the rock surface and the nonwetting fluid flows in the central
403 part of the pores (Fig. 3). Thus, the wetting fluid is mainly affected by interaction with the rock
404 surface, and the change in capillary force has a negligible effect. However, when Ca is low (\log
405 $Ca = -3.50$), the k_w decrease is more notable. This phenomenon can be attributed to the drag
406 force exerted by the nonwetting fluid. At $\log Ca = -3.50$, k_{nw} becomes notably lower compared
407 to other Ca conditions and the nonwetting fluid velocity is low. This result suggests that the
408 influence of the nonwetting fluid drag force on the wetting fluid increases, causing k_w to
409 markedly decrease with the k_{nw} decrease. Nevertheless, we conclude that the variation in k_w is
410 dominated by the fluid saturation in the system and is little affected by changes in IFT or Ca .

411 3.2 $M-Ca-k_{nw}$ color diagram

412 After confirming the influence of M and Ca on k_{nw} and k_w in a two-phase flow system,
413 we conducted simulations with various values of M and Ca at a constant 20% S_{nw} to create a M -
414 Ca - k_{nw} correlation diagram (Fig. 8). We chose the 20% S_{nw} condition because it is realistic under
415 all M - Ca conditions (Tsuji et al., 2016). We created the color diagram only for the nonwetting
416 fluid because the relative permeability curves (Fig. 7) demonstrate that k_w does not respond
417 markedly to changes in Ca . We also created a regression model and equation for our results
418 reported in this section (see Appendix B). The maximum Reynolds number reached in this set of
419 simulations was 3.92 for $M = 0.10$ and $\log Ca \approx 0$.

420 Color maps are useful to provide estimates of k_{nw} under a wide range of M and Ca
421 conditions in a reservoir and to analyze the degree of influence on k_{nw} by M and Ca (Fig. 8). The
422 first color map (Fig. 8a) depicts the parameter space of $\log M = -1.02$ to 0.70 and $\log Ca = -4.00$
423 to 0.00 , which represents the broad range of conditions that can be simulated. Values higher than
424 this range are hard to achieve at the field scale, and lower values are outside the stable range of
425 the simulation. The second color map (Fig. 8b), covering the lower left quadrant of the parameter
426 range shown in Fig. 8a with parameter space of $\log M = -1.02$ to 0.00 and $\log Ca = -4.00$ to -
427 1.00 , was produced to increase the accuracy of k_{nw} estimates for a system with low M and low
428 Ca , which is common in CCS field.

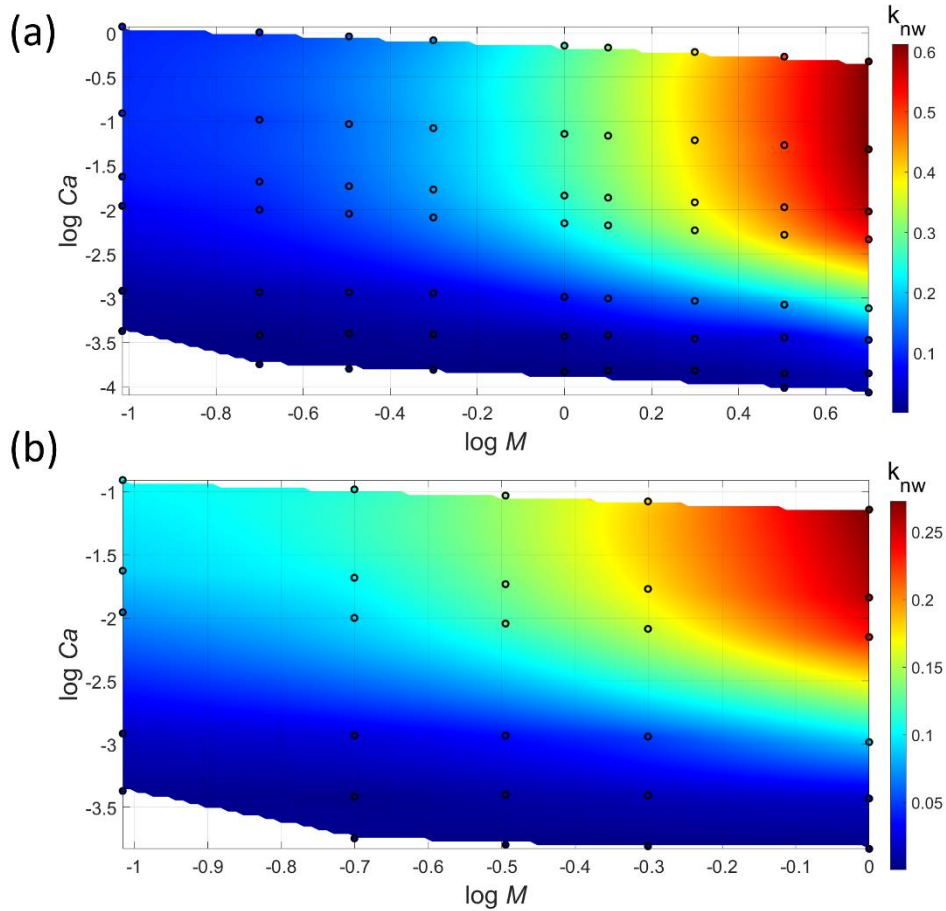


Fig. 8. Relative permeability map of the nonwetting fluid for (a) $\log M = -1.02$ to 0.70 and $\log Ca = -4.00$ to 0.00, and (b) $\log M = -1.02$ to 0.00 and $\log Ca = -4.00$ to -1.00 . The dots indicate the Ca - M conditions used for LBM simulation.

429

430

431

432

433

434

435

436

437

In the specified parameter range, k_{nw} varies from 0.0002 to 0.6125 (Fig. 8a). For high $\log Ca$ values (between -1.25 to 0.00), k_{nw} does not vary with $\log Ca$ and is only influenced by M , as indicated by the almost straight vertical borders between color bands. This finding agrees with our results from section 3.1.2 (Fig. 7), which shows that for $\log Ca \geq -1.25$, the nonwetting fluid relative permeability curve is not affected by Ca . However, as $\log Ca$ becomes lower than -1.25 (Ca value ≈ 0.06), k_{nw} can be seen to vary on both the x axis ($\log M$) and the y axis ($\log Ca$), that is, k_{nw} starts to be affected by the capillary force. The diagram agrees with our finding in section 3.2 that for $\log Ca$ lower than -1.25 , k_{nw} decreases as Ca decreases.

438 The k_{nw} variation with M (x axis) is more pronounced for $\log M > 0$ ($M > 1$) than for \log
439 $M < 0$ (Fig. 8a). This result is consistent with our findings in section 3.1 and is caused by the
440 lubrication effect resulting from viscosity differences. When μ_{nw} is higher than μ_w , the resulting
441 instability and viscous coupling effect enhance the relative permeability of the nonwetting fluid.
442 The diagram clearly captures the contrast between k_{nw} at $\log M < 0$ and at $\log M > 0$.

443 To check the detailed k_{nw} variation under low M and low Ca conditions, in Fig. 8b we
444 show an enlargement of part of the lower left quadrant of the parameter range illustrated in Fig.
445 8a. The k_{nw} value range is 0.0002 to 0.2725 in Fig. 8b, and in this parameter space, both Ca and
446 M influence k_{nw} and thus the borders between the color bands are curved. In a CCS field, M is
447 usually lower than 1 and Ca is generally low (Zheng et al., 2017). Therefore, Fig. 8b is useful for
448 estimating nonwetting fluid relative permeability in a CCS field.

449 The diagram is useful for evaluating k_{nw} when the effects of M and Ca are considered
450 simultaneously, and the graph neatly summarizes all the main results of this study. The diagram
451 shows that capillary force starts affecting the flow of the nonwetting fluid when $\log Ca$ is less
452 than -1.25 and that the effect of changes in Ca may be just as important as that of changes in M .
453 The graph also shows that k_{nw} is affected by M under all conditions, but most markedly when \log
454 $M > 0$. The graph yields a good estimate of k_{nw} at 20% saturation based on the M and Ca
455 parameters.

456 **4 Discussion**

457 We have demonstrated how M and Ca can markedly change the relative permeabilities of
458 the nonwetting and wetting fluids in a reservoir; thus, our results can help identify the optimum
459 properties of the immiscible fluids to be used in a geologic reservoir. For example, in a CCS

460 project, the injectivity of the CO₂ is highest when the reservoir fluid has a lower viscosity and the
461 IFT between the two fluids is low. Thus, the relative permeability of injected CO₂ is higher in a
462 saline aquifer than in an oil field. For an EOR project, the relative permeability of oil is higher
463 when a fluid with low viscosity is injected.

464 The relative permeability map (Fig. 8) is useful to provide accurate estimates of k_{nw} in
465 reservoir-scale simulations. Currently, the relative permeabilities of the nonwetting and wetting
466 fluid are simulated on the basis of a uniform relative permeability curve, without regard to the M
467 and Ca conditions. However, we have shown that the nonwetting fluid, at a typical saturation
468 (S_{nw}) of 20%, can vary in relative permeability by an order of magnitude, from 0.0002 to 0.6125,
469 depending on M and Ca conditions. The color map created in this study can provide more
470 accurate estimates of relative permeability (e.g., temporal permeability variations in a 3D
471 reservoir model) if Ca and M are derived from the reservoir simulation. In addition, although the
472 M generally remains constant in the two-phase flow, the Ca value can greatly changes depending
473 on the distance from the injection well in a reservoir. For example, when evaluating the reservoir
474 area located near the injection well, the injection pressure creates a high-pressure gradient which
475 causes the injected fluid velocity to be high. As the fluid flows away from the injection site, the
476 fluid velocity becomes slower, thus the Ca becomes lower. This means that fluid relative
477 permeability varies based on location inside the reservoir, and the permeability variation can be
478 evaluated using the relative permeability map, thus providing a more accurate relative
479 permeability estimation.

480 In this study, we conducted the simulation under steady-state conditions, as being most
481 representative for illustrating fluid flows in a reservoir area distant from the injection site, where
482 boundary effects are negligible (Honarpour et al., 2018; Ramstad et al., 2012). In addition, under

483 steady-state conditions, relative permeability can be measured directly by using Darcy's law;
484 thus, the relative permeability value is more accurate than one calculated under non-steady-state
485 conditions. However, there are some differences between relative permeability values obtained
486 under steady-state and non-steady-state conditions, and there are also some limitations to steady-
487 state simulations. Under steady-state conditions, both fluid phases coexist together in the
488 reservoir at the prescribed saturation from the beginning of the simulation. In contrast, under
489 non-steady-state conditions, the reservoir is initially filled with wetting fluid, and nonwetting
490 fluid is injected and gradually displaces the wetting fluid, which results in a gradual increase of
491 nonwetting fluid saturation and a decrease of wetting fluid saturation. As a result, under non-
492 steady-state conditions several factors can affect relative permeability variation, such as
493 fingering phenomena, drainage and imbibition conditions, and the pore-filling behavior during
494 the injection (Bakhshian et al., 2021; Rabbani et al., 2017). Therefore, an unsteady-state
495 simulation can better represent relative permeability near the borehole or injection site, where
496 remarkable displacement occurs. Nevertheless, if considering the law of two-phase fluid flow
497 that coexist and flow together throughout the whole drainage area, steady-state relative
498 permeability curves are more suitable for planning the whole reservoir design. In addition,
499 relative permeability obtained under steady-state conditions is more accurate because the relative
500 permeability can be directly measured by using Darcy's law. In contrast, in an unsteady-state
501 simulation, relative permeability must be calculated from the capillary pressure change and
502 production data under several assumptions (e.g., the Johnson, Bossler, and Naumann method;
503 (Esmaeili et al., 2020; Johnson et al., 1959)). As a result, the obtained relative permeability is
504 less accurate. Steady-state condition is also better to estimate relative permeability for CCS

505 monitoring system after injection, as at the time, the CO₂ will coexist with the wetting fluid in
506 the reservoir.

507 In this study, we created a relative permeability map for $S_{nw} = 20\%$, which is a reasonable
508 condition that can be achieved in all or most systems. As S_{nw} increases, k_{nw} also increases until it
509 reaches its maximum value (e.g., k_{nw} at the irreducible saturation). Therefore, it is advisable to
510 create relative permeability maps for several saturation conditions. One possible future direction
511 from this study would be to create a four-dimensional $M-Ca-S_{nw}-k_{nw}$ graph to yield k_{nw}
512 estimates for all saturation conditions. Nevertheless, the great consistency of variations in k
513 caused by changes in M and Ca found in this study suggests that maps for other saturation
514 conditions will have similar features to Fig. 8. It would also be possible to create a regression
515 model for $k_{nw} = f(M-Ca-S_{nw})$ to estimate k_{nw} under all saturation conditions.

516 In this study, we produced a relative permeability diagram for a digital specimen of Berea
517 sandstone. In addition to M and Ca , the influences upon relative permeability include the pore
518 geometry of the rock, such as pore size distribution, pore connectivity, and other parameters
519 (Jiang et al. 2018, WRR). These parameters differ among rock formations, meaning that the
520 relative permeability maps of different types of reservoir rocks will vary. Our methodology
521 makes it possible to create accurate maps of relative permeability for other reservoir rocks.

522 In this study, we used $\log M$ ranging from -1.02 to 0.70 and $\log Ca$ ranging from -4.00
523 to 0.00 ; however, in the CO₂ injection process, $\log M$ might reach as low as -1.8 and $\log Ca$
524 might reach -6.8 (Zheng et al., 2017). Such values are outside the stable range where this
525 simulation can be applied. Nevertheless, the objective of this study was just to propose a method
526 to predict the relative permeability of a two-phase flow fluid in a reservoir by using a color map
527 diagram to evaluate the effect of the viscosity ratio and capillary number (Fig. 8). In a future

528 study, we plan to improve the stability range of the simulation to allow lower M and Ca values to
529 be considered.

530 In geological CO₂ storage, the maximum amount of CO₂ that can be stored and the
531 injectivity of the CO₂ into the reservoir must both be considered (Tsuji et al., 2016). Thus, the
532 results of this study must be combined with information on the effects of M and Ca on the
533 maximum saturation of the nonwetting fluid. In this study, we showed that, for CO₂ as the
534 nonwetting fluid, the relative permeability increases as M increases and decreases as Ca becomes
535 very small. In contrast, Tsuji et al. (2016) demonstrated that the maximum S_{nw} increases as M
536 increases and notably increases at low Ca . Thus, although a high value of M is desirable to
537 increase both the CO₂ capacity and injectivity, a low Ca value can also increase the maximum
538 CO₂ saturation but at the cost of reduced relative permeability. Both factors must be taken into
539 account when choosing suitable conditions for CO₂ storage.

540 An advantage of using M and Ca is that both parameters are dimensionless, meaning that
541 the results obtained in this pore-scale study can potentially be upscaled to the reservoir scale.
542 Ideally, the pore-scale results are also valid at the reservoir scale as long as the ratios of the
543 parameters (viscosity and IFT) are maintained for both fluids, because the fluid flow behavior at
544 the reservoir scale is controlled by the fluid dynamics at the pore scale. However, this ideal is
545 challenged by the inhomogeneity of the porous medium. The relative permeability is likely to
546 vary throughout the reservoir due to differences in pore size, pore connectivity, and many other
547 factors. Nevertheless, the results of a pore-scale simulation are important to verify relative
548 permeability variations arising from selected factors (in this study, M and Ca) by eliminating
549 other factors. The results of a pore-scale study of relative permeability could then be upscaled by

550 considering the structural factors of the reservoir, e.g., its porosity and pore connectivity, using
551 advanced techniques such as machine learning.

552 **5 Summary**

553 To evaluate the influence of viscosity ratio M and capillary number Ca on relative
554 permeability k in a two-phase flow system, we calculated k for nonwetting and wetting fluids
555 (k_{nw} and k_w) under various M and Ca conditions using an LBM simulation. The main results of
556 this study are as follows.

- 557 1) In our simulations, the relative permeability of the nonwetting fluid increased as the
558 viscosity ratio increased due to the lubricating effect, locally occurred pore-filling
559 behavior, and instability of the fluid interface. Specifically, at high viscosity ratios ($M =$
560 5), k_{nw} could exceed 1 as a result of the lubricating effect.
- 561 2) The relative permeability of the wetting fluid decreased as M increased due to the
562 increase in shear force from the nonwetting fluid (viscous coupling effect)
- 563 3) As M increased, the number nonwetting fluid clusters became higher, indicating that the
564 nonwetting fluid became more disconnected and the size of each clusters becomes
565 smaller.
- 566 4) At high capillary numbers ($\log Ca = -0.25$ to -1.25), k_{nw} did not respond to Ca , however
567 as $\log Ca$ becomes lower than -1.25 , k_{nw} decreases as Ca decreases due to the capillary
568 force effect.
- 569 5) As Ca decreased k_w decreased, but at a negligible rate compared to k_{nw} .

570 6) k_{nw} can change markedly in a wide range of $M-Ca$ parameter space, and the $M-Ca-k_{nw}$
571 correlation map created in this study can provide k_{nw} estimates at various reservoir
572 conditions.

573 **Acknowledgements**

574 This study was supported by the Japan Society for the Promotion of Science (JSPS) through a
575 Grant-in-Aid for Challenging Exploratory Research (Grant Number JP20K20948). This work
576 was also partially supported by the JSPS KAKENHI Grant Number JP19K15100. We are
577 grateful for the funding provided by the Top Global University project conducted by the Ministry
578 of Education, Culture, Sports, and Technology, Japan (MEXT). We also gratefully acknowledge
579 support of International Institute for Carbon-Neutral Energy Research (I²CNER). The Micro-CT
580 data used to reconstruct the digital rock model is achieved by The Imperial College Consortium
581 on Pore-Scale Modelling and Imaging.

582 **Appendices**

583 A. Single-phase simulation

584 Before conducting the two-phase flow simulations, we first ran single-phase simulations
585 to calculate the absolute permeability of the 3D rock model. Single-phase simulations can also be
586 used to verify the accuracy and precision of the simulation. When only one type of fluid exists in
587 a rock, the absolute permeability can be calculated from Darcy's law:

$$588 \quad k = \frac{v \mu \Delta l}{\Delta P} \quad (\text{A. 1})$$

589 where k is the absolute permeability (m^2), v is the average fluid velocity (m/s), μ is the dynamic
590 viscosity of the fluid (Pa s), Δl is the distance between the inlet and the outlet, and ΔP is the

591 applied pressure difference between the inlet and the outlet. In this study, because the body force
 592 was applied only in the z direction, we calculated k in the z direction (k_z).

593 Because all simulation units are in lattice Boltzmann units, they must subsequently be
 594 converted into physical units. The unit conversion for k can be performed using the formula:

$$595 \quad k_{(physical)} = k_{(LB)} * A^2 \quad (A. 2)$$

596 where A is the resolution of the digital rock, i.e. the physical size of a lattice grid (2.673 μm in
 597 this study).

598 Absolute permeability is an intrinsic property of a rock that is independent of the type of
 599 fluid. The single-phase simulations were conducted with several different values of fluid
 600 viscosity and body force to ensure the consistency of the results. When the fluid summation of
 601 velocity change in 1,000 steps difference was less than 2% for all cases, the simulations were
 602 assumed to have converged at that time. The absolute permeability results in various viscosity
 603 and body force conditions are shown in the table A.1.

| kinematic viscosity (lattice-Boltzmann unit) | Body force (lattice-Boltzmann unit) | absolute permeability (Darcy) |
|---|--|--|
| 0.155555 | 0.0001 | 1.3029 |
| 0.155555 | 0.0002 | 1.3025 |
| 0.310000 | 0.0001 | 1.3042 |
| 0.310000 | 0.0002 | 1.3038 |

604 Table A.1 single-phase simulation conditions and results

605 The absolute permeability of the Berea rock is 1.3034 ± 0.001 Darcy. The absolute
 606 permeability value remains constant under various conditions, which demonstrates the accuracy
 607 and stability of the simulation. The result obtained from this simulation is slightly different from

608 the result by the Dong and Blunt (2009), which gives the absolute permeability value of 1.193
609 Darcy. The difference might be due to the difference in size of digital rocks. Dong and Blunt
610 used digital rock with dimension of 400x400x400 voxels with resolution of 5.345 μm (9.772
611 mm^3 in actual size), while we used digital rock with dimension of 400x400x400 voxels with
612 resolution of 2.673 μm (1.222 mm^3 in actual size) is used. The dimension difference might have
613 caused a slight change in the rock sample heterogeneity. In addition, Dong and Blunt applied
614 Pore Network Model (PNM) to calculate the absolute permeability, while in this study, LBM
615 simulation is used. Nonetheless, the absolute permeability value obtained is still in the same
616 order as described by the paper.

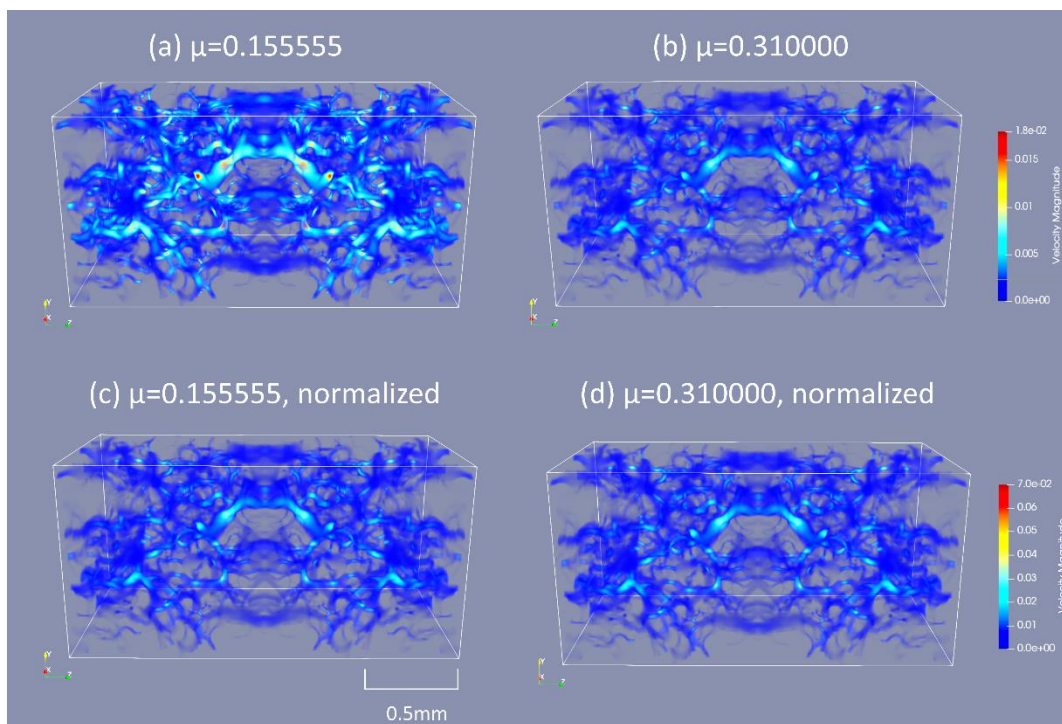


Fig. A. Velocity fields for single phase simulation at (a) $\mu = 0.155555$ and (b) $\mu = 0.310000$ and normalized velocity fields for single phase simulation at (c) $\mu = 0.155555$ and (d) $\mu = 0.310000$.

617

618 We show the velocity field of single-phase simulation for kinematic viscosity = 0.155555
619 and 0.310000 with equal body force of 0.0001 (Fig. A(a) and A(b)). The fluid velocity for
620 simulation with fluid kinematic viscosity of 0.155555 nu_{LB} is significantly higher compared
621 to the fluid kinematic viscosity of 0.310000 nu_{LB} case. This is because fluid average
622 velocity is inversely proportional to viscosity. Thus, fluid velocity is not proportional to
623 permeability, and must be normalized into dimensionless velocity field. Fig. A(c) and A(d) show
624 the normalized fluid velocity field for both conditions. The normalization is done using the
625 equation $U^* = \frac{U}{\Delta PL/\mu}$. Both figures show a relatively similar results, which indicate that a similar
626 absolute permeability value is obtained from both conditions.

627

628 B. Regression model of the M - Ca - k_{nw} relationship

629 We created a regression model to generate an empirical equation that can be used to
630 calculate k_{nw} as a function of M and $\log Ca$ at 20% S_{nw} . A height map of our simulation results
631 and the fitted polynomial regression curve is shown in Fig. B.

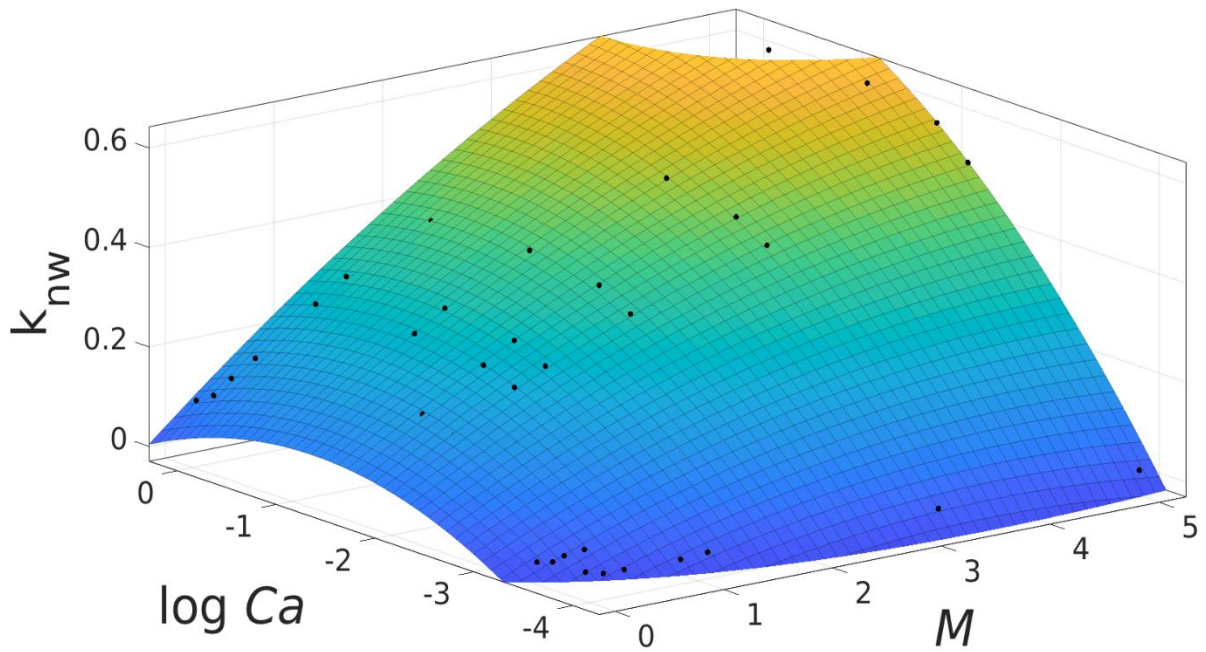


Fig. B. Nonwetting fluid relative permeability height map (dots) and the fitted polynomial regression curve.

632

633 Past research has shown that k_{nw} can be estimated as a function of M by using an equation
 634 with second-degree polynomial (equation 3 and 4 (Goldsmith & Mason, 1963)); thus, we chose a
 635 second polynomial equation for the regression towards the M value. For the $\log Ca$ value, we
 636 also set it as second-degree polynomial to prevent overfitting.

637 Based on our model, k_{nw} can be calculated with the following formula:

638

$$639 \quad k_{nw} = 0.05983 + 0.1844 M - 0.08714 (\log Ca) - 0.009922 M^2 + 0.0275M(\log Ca)$$

$$640 \quad \quad \quad - 0.03335 (\log Ca)^2$$

641

642 Our model has an R -squared value of 0.9481 and a summed square of residuals value of
 643 0.09871.

644 Because we created a color map diagram for only one saturation condition ($S_{nw} = 20\%$),
 645 we only created a regression model to calculate k_{nw} based on M and Ca values for this saturation
 646 condition. Because the relative permeability increase with respect to saturation is not linear, we
 647 expect the regression model to be different for other saturation conditions. In the future, we plan
 648 to create more relative permeability color maps for various saturation conditions and create a
 649 four-dimensional $\log M$ – $\log Ca$ – S_{nw} – k_{nw} graph to yield k_{nw} estimates for all saturation
 650 conditions. Then, we will attempt to create a regression model to estimate k_{nw} as a function of M ,
 651 $\log Ca$, and S_{nw} .

652

653 **References**

- 654 Ahmadiouydarab, M., Liu, Z. S., & Feng, J. J. (2012). International Journal of Multiphase Flow
 655 Relative permeability for two-phase flow through corrugated tubes as model porous media.
 656 *International Journal of Multiphase Flow*, 47, 85–93.
 657 <http://dx.doi.org/10.1016/j.ijmultiphaseflow.2012.07.005>
- 658 Ahrenholz, B., Tölke, J., Lehmann, P., Peters, A., Kaestner, A., Krafczyk, M., & Durner, W.
 659 (2008). Prediction of capillary hysteresis in a porous material using lattice-Boltzmann
 660 methods and comparison to experimental data and a morphological pore network model.
 661 *Advances in Water Resources*, 31(9), 1151–1173.
 662 <https://doi.org/10.1016/j.advwatres.2008.03.009>
- 663 Amaefule, J. O., & Handy, L. L. (1982). The Effect of Interfacial Tensions on Relative
 664 Oil/Water Permeabilities of Consolidated Porous Media. *Society of Petroleum Engineers*
 665 *Journal*, 22(03), 371–381. <https://doi.org/10.2118/9783-PA>
- 666 Asar, H., & Handy, L. L. (1989). Influence of interfacial tension on gas/oil relative permeability
 667 in a gas-condensate system. *Spe Reservoir Engng.*, 3(1, Feb. 1989), 257–264.
 668 <https://doi.org/10.2118/11740-pa>
- 669 Bakhshian, S., Rabbani, H. S., & Shokri, N. (2021). Physics-Driven Investigation of Wettability
 670 Effects on Two-Phase Flow in Natural Porous Media: Recent Advances, New Insights, and
 671 Future Perspectives. *Transport in Porous Media*, 140(1), 85–106.
 672 <https://doi.org/10.1007/s11242-021-01597-z>
- 673 Bear, J. (1975). Dynamics of Fluids in Porous Media: *Soil Science*, 120(2), 162–163.

- 674 <https://doi.org/10.1097/00010694-197508000-00022>
- 675 Benson, S. M., Hingerl, F., Zuo, L., Krevor, S., Reynolds, C., Niu, B., Calvo, R., Niemi, A., Pini,
676 R., Krevor, S., Reynolds, C., Niu, B., Calvo, R., & Niemi, A. (2015). Relative permeability
677 for multi-phase flow in CO₂ storage reservoirs. Part II: resolving fundamental issues and
678 filling data gaps. *Global CCS Institute, December*, 1–52.
- 679 Bischofberger, I., Ramachandran, R., & Nagel, S. R. (2015). An island of stability in a sea of
680 fingers: emergent large-scale features of the viscous flow instability. *ArXiv:1410.7623*
681 [*Physics*]. <http://arxiv.org/abs/1410.7623>
- 682 Burnside, N. M., & Naylor, M. (2014). International Journal of Greenhouse Gas Control Review
683 and implications of relative permeability of CO₂ / brine systems and residual trapping of
684 CO₂. *International Journal of Greenhouse Gas Control*, 23, 1–11.
685 <https://doi.org/10.1016/j.ijggc.2014.01.013>
- 686 Chen, C., & Zhang, D. (2010). Pore-scale simulation of density-driven convection in fractured
687 porous media during geological CO₂ sequestration. *Water Resources Research*, 46(11).
688 <https://doi.org/https://doi.org/10.1029/2010WR009453>
- 689 Chen, S., & Doolen, G. D. (1998). LATTICE BOLTZMANN METHOD FOR FLUID FLOWS.
690 *Annual Review of Fluid Mechanics*, 30(1), 329–364.
691 <https://doi.org/10.1146/annurev.fluid.30.1.329>
- 692 Dong, H., & Blunt, M. J. (2009). Pore-network extraction from micro-computerized-tomography
693 images. *Physical Review E*, 80(3), 36307. <https://doi.org/10.1103/PhysRevE.80.036307>
- 694 Dou, Z., & Zhou, Z. F. (2013). Numerical study of non-uniqueness of the factors influencing
695 relative permeability in heterogeneous porous media by lattice Boltzmann method.
696 *International Journal of Heat and Fluid Flow*, 42, 23–32.
697 <https://doi.org/10.1016/j.ijheatfluidflow.2013.01.020>
- 698 Esmaeili, S., Modaresghazani, J., Sarma, H., Harding, T., & Maini, B. (2020). Effect of
699 temperature on relative permeability – Role of viscosity ratio. *Fuel*, 278.
700 <https://doi.org/10.1016/j.fuel.2020.118318>
- 701 Fan, M., Dalton, L. E., McClure, J., Ripepi, N., Westman, E., Crandall, D., & Chen, C. (2019).
702 Comprehensive study of the interactions between the critical dimensionless numbers
703 associated with multiphase flow in 3D porous media. *Fuel*, 252, 522–533.
704 <https://doi.org/10.1016/j.fuel.2019.04.098>
- 705 Fulcher, R. A., Ertekin, T., & Stahl, C. D. (1985). Effect of Capillary Number and Its
706 Constituents on Two-Phase Relative Permeability Curves. *JPT, Journal of Petroleum*
707 *Technology*, 37(2), 249–260. <https://doi.org/10.2118/12170-PA>
- 708 Goel, G., Abidoye, L. K., Chahar, B. R., & Das, D. B. (2016). Scale dependency of dynamic
709 relative permeability–saturation curves in relation with fluid viscosity and dynamic
710 capillary pressure effect. *Environmental Fluid Mechanics*, 16(5), 945–963.
711 <https://doi.org/10.1007/s10652-016-9459-y>
- 712 Goldsmith, H. L., & Mason, S. G. (1963). The flow of suspensions through tubes. II. Single large
713 bubbles. *Journal of Colloid Science*, 18(3), 237–261. [https://doi.org/10.1016/0095-](https://doi.org/10.1016/0095-8522(63)90015-1)
714 [8522\(63\)90015-1](https://doi.org/10.1016/0095-8522(63)90015-1)

- 715 Gudjonsdottir, M., Palsson, H., Eliasson, J., & Saevarsdottir, G. (2015). Calculation of relative
716 permeabilities from field data and comparison to laboratory measurements. *Geothermics*,
717 *54*, 1–9. <https://doi.org/10.1016/j.geothermics.2014.10.004>
- 718 Harbert, L. W. (1983). Low interfacial tension relative permeability. *Proceedings - SPE Annual*
719 *Technical Conference and Exhibition, 1983-October*, 2–9. <https://doi.org/10.2523/12171-ms>
- 720 Heins, R., Simjoo, M., Zitha, P. L., & Rossen, W. R. (2014). Oil Relative Permeability During
721 Enhanced Oil Recovery by Foam Flooding. In *SPE Annual Technical Conference and*
722 *Exhibition*. <https://doi.org/10.2118/170810-MS>
- 723 Honarpour, M., Koederitz, L., & Harvey, A. (2018). Relative Permeability of Petroleum
724 Reservoirs. In *Relative Permeability of Petroleum Reservoirs*.
725 <https://doi.org/10.1201/9781351076326>
- 726 Huang, H., & Lu, X. Y. (2009). Relative permeabilities and coupling effects in steady-state gas-
727 liquid flow in porous media: A lattice Boltzmann study. *Physics of Fluids*, *21*(9).
728 <https://doi.org/10.1063/1.3225144>
- 729 Huang, H., Sukop, M. C., & Lu, X.-Y. (2015). Rothman–Keller multiphase Lattice Boltzmann
730 model. In *Multiphase Lattice Boltzmann Methods: Theory and Application* (pp. 94–135).
731 <https://doi.org/https://doi.org/10.1002/9781118971451.ch4>
- 732 Huang, H., Wang, L., & Lu, X. Y. (2011). Evaluation of three lattice Boltzmann models for
733 multiphase flows in porous media. *Computers and Mathematics with Applications*, *61*(12),
734 3606–3617. <https://doi.org/10.1016/j.camwa.2010.06.034>
- 735 Jeong, G. S., Lee, J., Ki, S., Huh, D. G., & Park, C. H. (2017). Effects of viscosity ratio,
736 interfacial tension and flow rate on hysteric relative permeability of CO₂/brine systems.
737 *Energy*, *133*, 62–69. <https://doi.org/10.1016/j.energy.2017.05.138>
- 738 Jiang, F., & Tsuji, T. (2017). Estimation of three-phase relative permeability by simulating fluid
739 dynamics directly on rock-microstructure images: ESTIMATION OF THREE-PHASE
740 PERMEABILITY. *Water Resources Research*, *53*(1), 11–32.
741 <https://doi.org/10.1002/2016WR019098>
- 742 Jiang, Fei, Liu, H., Chen, X., & Tsuji, T. (2022). A coupled LBM-DEM method for simulating
743 the multiphase fluid-solid interaction problem. *Journal of Computational Physics*, *454*,
744 110963. <https://doi.org/10.1016/j.jcp.2022.110963>
- 745 Jiang, Fei, & Tsuji, T. (2014). Changes in pore geometry and relative permeability caused by
746 carbonate precipitation in porous media. *Physical Review E*, *90*(5), 53306.
747 <https://doi.org/10.1103/PhysRevE.90.053306>
- 748 Jiang, Fei, & Tsuji, T. (2016). Numerical investigations on the effect of initial state CO₂
749 topology on capillary trapping efficiency. *International Journal of Greenhouse Gas*
750 *Control*, *49*, 179–191. <https://doi.org/10.1016/j.ijggc.2016.03.006>
- 751 Jiang, Fei, Tsuji, T., & Hu, C. (2014). Elucidating the Role of Interfacial Tension for
752 Hydrological Properties of Two-Phase Flow in Natural Sandstone by an Improved Lattice
753 Boltzmann Method. *Transport in Porous Media*, *104*(1), 205–229.
754 <https://doi.org/10.1007/s11242-014-0329-0>

- 755 Jiang, Fei, Yang, J., Boek, E., & Tsuji, T. (2021). Investigation of viscous coupling effects in
756 three-phase flow by lattice Boltzmann direct simulation and machine learning technique.
757 *Advances in Water Resources*, *147*, 103797.
758 <https://doi.org/10.1016/j.advwatres.2020.103797>
- 759 Johnson, E. F., Bossler, D. P., & Bossler, V. O. N. (1959). Calculation of Relative Permeability
760 from Displacement Experiments. *Transactions of the AIME*, *216*(01), 370–372.
761 <https://doi.org/10.2118/1023-G>
- 762 Lefebvre du Prey, E. J. (1973). Factors Affecting Liquid-Liquid Relative Permeabilities of a
763 Consolidated Porous Medium. *Society of Petroleum Engineers Journal*, *13*(01), 39–47.
764 <https://doi.org/10.2118/3039-PA>
- 765 Lenormand, R., Touboul, E., & Zarcone, C. (1988). Numerical models and experiments on
766 immiscible displacements in porous media. *Journal of Fluid Mechanics*, *189*, 165–187.
767 <https://doi.org/10.1017/S0022112088000953>
- 768 Li, H., Pan, C., & Miller, C. T. (2005). Pore-scale investigation of viscous coupling effects for
769 two-phase flow in porous media. *Physical Review E - Statistical, Nonlinear, and Soft Matter*
770 *Physics*, *72*(2), 1–14. <https://doi.org/10.1103/PhysRevE.72.026705>
- 771 Li, X., Jiang, F., & Hu, C. (2016). Analysis of the accuracy and pressure oscillation of the lattice
772 Boltzmann method for fluid–solid interactions. *Computers & Fluids*, *129*, 33–52.
773 <https://doi.org/10.1016/j.compfluid.2016.01.015>
- 774 Mahmoudi, S., Mohammadzadeh, O., Hashemi, A., & Kord, S. (2017). Pore-scale numerical
775 modeling of relative permeability curves for CO₂–oil fluid system with an application in
776 immiscible CO₂ flooding. *Journal of Petroleum Exploration and Production Technology*,
777 *7*(1), 235–249. <https://doi.org/10.1007/s13202-016-0256-4>
- 778 McDougall, S. R., Salino, P. A., & Sorbie, K. S. (2007). *The Effect of Interfacial Tension Upon*
779 *Gas-Oil Relative Permeability Measurements: Interpretation Using Pore-Scale Models*.
780 <https://doi.org/10.2523/38920-ms>
- 781 Mu'min, G. F., Kawaguchi, T. (川口 達也), & Saito, T. (齊藤 卓志). (2021). Droplet breakup
782 of a high-viscosity-ratio system in a nonuniform temperature field under laser irradiation.
783 *Physics of Fluids*, *33*(7), 73108. <https://doi.org/10.1063/5.0055235>
- 784 Nekouei, M., & Vanapalli, S. A. (2017). Volume-of-fluid simulations in microfluidic T-junction
785 devices: Influence of viscosity ratio on droplet size. *Physics of Fluids*, *29*(3), 32007.
786 <https://doi.org/10.1063/1.4978801>
- 787 Niibori, Y., Ahn, J., & Mimura, H. (2011). Uncertainty of Relative Permeability to Describe
788 Two-Phase Flow in Geological Disposal System. *Nuclear Technology*, *175*(3), 641–651.
789 <https://doi.org/10.13182/NT11-A12512>
- 790 Odeh, A. S. (1959). Effect of Viscosity Ratio on Relative Permeability (includes associated
791 paper 1496-G). *Transactions of the AIME*, *216*(01), 346–353. [https://doi.org/10.2118/1189-](https://doi.org/10.2118/1189-G)
792 [G](https://doi.org/10.2118/1189-G)
- 793 Øren, P. E., & Bakke, S. (2003). Reconstruction of Berea sandstone and pore-scale modelling of
794 wettability effects. *Journal of Petroleum Science and Engineering*, *39*(3–4), 177–199.

- 795 [https://doi.org/10.1016/S0920-4105\(03\)00062-7](https://doi.org/10.1016/S0920-4105(03)00062-7)
- 796 Rabbani, H. S., Joekar-Niasar, V., Pak, T., & Shokri, N. (2017). New insights on the complex
797 dynamics of two-phase flow in porous media under intermediate-wet conditions. *Scientific*
798 *Reports*, 7(1), 4584. <https://doi.org/10.1038/s41598-017-04545-4>
- 799 Ramstad, T., Idowu, N., Nardi, C., & Øren, P.-E. (2012). Relative Permeability Calculations
800 from Two-Phase Flow Simulations Directly on Digital Images of Porous Rocks. *Transport*
801 *in Porous Media*, 94(2), 487–504. <https://doi.org/10.1007/s11242-011-9877-8>
- 802 Ramstad, T., Øren, P. E., & Bakke, S. (2010). Simulation of two-phase flow in Reservoir rocks
803 using a lattice Boltzmann method. *SPE Journal*, 15(4), 923–933.
804 <https://doi.org/10.2118/124617-pa>
- 805 Shad, S., Gates, I. D., & Maini, B. B. (2008). Experimental study of heavy oil-water flow
806 structure effects on relative permeabilities in a fracture filled with heavy oil. *Society of*
807 *Petroleum Engineers - International Thermal Operations and Heavy Oil Symposium,*
808 *ITOHOS 2008 - "Heavy Oil: Integrating the Pieces,"* 2, 690–701.
809 <https://doi.org/10.2118/117644-ms>
- 810 Shen, P., Zhu, B., Li, X. Bin, & Wu, Y. S. (2010). An Experimental Study of the Influence of
811 Interfacial Tension on Water-Oil Two-Phase Relative Permeability. *Transport in Porous*
812 *Media*, 85(2), 505–520. <https://doi.org/10.1007/s11242-010-9575-y>
- 813 Singh, S., Jiang, F., & Tsuji, T. (2017). Influence of Slip Flow at Fluid-solid Interface upon
814 Permeability of Natural Rock. *Energy Procedia*, 114, 3572–3577.
815 <https://doi.org/10.1016/j.egypro.2017.03.1487>
- 816 Stone, H. A. (1994). Dynamics of Drop Deformation and Breakup in Viscous Fluids. *Annual*
817 *Review of Fluid Mechanics*, 26(1), 65–102.
818 <https://doi.org/10.1146/annurev.fl.26.010194.000433>
- 819 Succi, S., Sbragaglia, M., & Ubertini, S. (2010). Lattice Boltzmann Method. *Scholarpedia*, 5(5),
820 9507. <https://doi.org/10.4249/scholarpedia.9507>
- 821 Tölke, J., Freudiger, S., & Krafczyk, M. (2006). An adaptive scheme using hierarchical grids for
822 lattice Boltzmann multi-phase flow simulations. *Computers & Fluids*, 35(8), 820–830.
823 <https://doi.org/https://doi.org/10.1016/j.compfluid.2005.08.010>
- 824 Tsuji, T., Jiang, F., & Christensen, K. T. (2016). Characterization of immiscible fluid
825 displacement processes with various capillary numbers and viscosity ratios in 3D natural
826 sandstone. *Advances in Water Resources*, 95, 3–15.
827 <https://doi.org/10.1016/j.advwatres.2016.03.005>
- 828 Vafai, K. (2000). *Handbook of Porous Media*. Marcel Dekker, Inc.
- 829 Wu, Q., & Wang, J. (2020). A thermo-hydro-mechanical coupling analysis for the contaminant
830 transport in a bentonite barrier with variable saturation. *Water (Switzerland)*, 12(11), 1–23.
831 <https://doi.org/10.3390/w12113114>
- 832 Yang, J., & Boek, E. S. (2013). A comparison study of multi-component Lattice Boltzmann
833 models for flow in porous media applications. *Computers and Mathematics with*
834 *Applications*, 65(6), 882–890. <https://doi.org/10.1016/j.camwa.2012.11.022>

- 835 Yiantsios, S. G., & Higgins, B. G. (1988). Numerical solution of eigenvalue problems using the
836 compound matrix method. *Journal of Computational Physics*, 74(1), 25–40.
837 [https://doi.org/10.1016/0021-9991\(88\)90066-6](https://doi.org/10.1016/0021-9991(88)90066-6)
- 838 Yih, C. S. (1967). Instability due to viscosity stratification. *Journal of Fluid Mechanics*, 27(2),
839 337–352. <https://doi.org/10.1017/S0022112067000357>
- 840 Yiotis, A. G., Psihogios, J., Kainourgiakis, M. E., Papaioannou, A., & Stubos, A. K. (2007). A
841 lattice Boltzmann study of viscous coupling effects in immiscible two-phase flow in porous
842 media. *Colloids and Surfaces A: Physicochemical and Engineering Aspects*, 300(1-2 SPEC.
843 ISS.), 35–49. <https://doi.org/10.1016/j.colsurfa.2006.12.045>
- 844 Zhang, Y., Jiang, F., & Tsuji, T. (2022). Influence of pore space heterogeneity on mineral
845 dissolution and permeability evolution investigated using lattice Boltzmann method.
846 *Chemical Engineering Science*, 247, 117048. <https://doi.org/10.1016/j.ces.2021.117048>
- 847 Zhao, H., Ning, Z., Kang, Q., Chen, L., & Zhao, T. (2017). Relative permeability of two
848 immiscible fluids flowing through porous media determined by lattice Boltzmann method.
849 *International Communications in Heat and Mass Transfer*, 85(May), 53–61.
850 <https://doi.org/10.1016/j.icheatmasstransfer.2017.04.020>
- 851 Zheng, X., Mahabadi, N., Yun, T. S., & Jang, J. (2017). Effect of capillary and viscous force on
852 CO₂ saturation and invasion pattern in the microfluidic chip. *Journal of Geophysical*
853 *Research: Solid Earth*, 122(3), 1634–1647.
854 <https://doi.org/https://doi.org/10.1002/2016JB013908>

855

856

857

858 **Figure Caption**

859 Fig. 1. Berea sandstone digital rock model: (a) core form and (b) mirrored form.

860

861 Fig. 2. Relative permeability curves as a function of M at constant $\log Ca = -0.25 \pm 0.1$ for $M = 0.1-5$: (a)
862 nonwetting fluid relative permeability (k_{nw}) curve and (b) wetting fluid relative permeability (k_w) curve.

863

864 Fig. 3. Two-dimensional slice showing the distributions of nonwetting fluid (red), wetting fluid (green),
865 and solid rock (black) at various values of M and S_{nw} .

866

867 Fig. 4. Evolution of the number of clusters of nonwetting fluid at $M = 1$ and $M = 5$, with $S_{nw} = 20\%$ and
868 $\log Ca = -0.25 \pm 0.1$.

869

870 Fig. 5. Two-dimensional slice showing the distributions of nonwetting (red), wetting fluid (green), and
871 solid rock (black) at (a) $M = 1$ and (b) $M = 5$ at 20% S_{nw} . These images show a portion of the slice
872 illustrated in Fig. 3.

873

874 Fig. 6. Normalized velocity fields for the nonwetting fluid in a two-phase simulation with (a) $M = 1$ and
875 (b) $M = 5$, at $\log Ca = -0.25 \pm 0.1$ and $S_{nw} = 20\%$.

876

877 Fig. 7. Relative permeability curves for the nonwetting (k_{nw} , green) and wetting fluids (k_w , blue) for \log
878 $Ca = -0.25$ to -3.5 with $M = 1$.

879

880 Fig. 8. Relative permeability map of the nonwetting fluid for (a) $\log M = -1.02$ to 0.70 and $\log Ca =$
881 -4.00 to 0.00 , and (b) $\log M = -1.02$ to 0.00 and $\log Ca = -4.00$ to -1.00 . The dots indicate the $Ca-M$
882 conditions used for LBM simulation.

883

884 Fig. A. Velocity fields for single phase simulation at (a) $\mu = 0.155555$ and (b) $\mu = 0.310000$ and
885 normalized velocity fields for single phase simulation at (c) $\mu = 0.155555$ and (d) $\mu = 0.310000$.

886

887 Fig. B. Nonwetting fluid relative permeability height map (dots) and the fitted polynomial regression
888 curve.

889

890

891

892